Publication II

Kari Astala, Jennifer L. Mueller, Lassi Päivärinta, Allan Perämäki and Samuli Siltanen. Direct electrical impedance tomography for nonsmooth conductivities. *Inverse Problems and Imaging*, Volume 5, Number 3, pages 531–549, doi:10.3934/ipi.2011.5.531, 2011.

Inverse Problems and Imaging
Volume 5, No. 3, 2011, 531–549
doi:10.3934/ipi.2011.5.531

DIRECT ELECTRICAL IMPEDANCE TOMOGRAPHY FOR NONSMOOTH CONDUCTIVITIES

Kari Astala

University of Helsinki
Department of Mathematics and Statistics
FI-00014 Helsinki, Finland

Jennifer L. Mueller

Colorado State University
Department of Mathematics and School of Biomedical Engineering
Fort Collins, CO 80523-1874, USA

Lassi Päivärinta

University of Helsinki
Department of Mathematics and Statistics
FI-00014 Helsinki, Finland

Allan Perämäki

Aalto University
Institute of Mathematics, P.O.Box 1100
FI-00076 Aalto, Finland

Samuli Siltanen

University of Helsinki
Department of Mathematics and Statistics
FI-00014 Helsinki, Finland

(Communicated by Giovanni Alessandrini)

Abstract. A new reconstruction algorithm is presented for EIT in dimension two, based on the constructive uniqueness proof given by Astala and Päivärinta in [*Ann. of Math.* **163** (2006)]. The method is non-iterative, provides a noise-robust solution of the full nonlinear EIT problem, and applies to more general conductivities than previous approaches. In particular, the new algorithm applies to piecewise smooth conductivities. Reconstructions from noisy and non-noisy simulated data from conductivity distributions representing a cross-sections of a chest and a layered medium such as stratified flow in a pipeline are presented. The results suggest that the new method can recover useful and reasonably accurate EIT images from data corrupted by realistic amounts of measurement noise. In particular, the dynamic range in medium-contrast conductivities is reconstructed remarkably well.

2000 *Mathematics Subject Classification.* Primary: 35R30, 65N21; Secondary: 65J20.

Key words and phrases. Inverse problem, Beltrami equation, Numerical solver, Conductivity equation, Inverse conductivity problem, Quasiconformal map, Complex geometrical optics solution, Nonlinear Fourier transform, Electrical impedance tomography.

1. **Introduction.** The aim of electrical impedance tomography (EIT) is to reconstruct the conductivity distribution inside an unknown physical body from electric boundary measurements. The reconstruction task is a nonlinear and ill-posed inverse problem. Applications of EIT include medical imaging, nondestructive testing, geophysical prospection and industrial process monitoring. See [11] for a general introduction to EIT.

We present a new computational EIT algorithm in dimension two based on the constructive uniqueness proof given by Astala and Päivärinta in [1, 2]. Our method is non-iterative, provides a noise-robust solution of the full nonlinear EIT problem, and assumes no regularity in the conductivity distribution contrary to previous direct EIT algorithms in the literature. In particular, our method is applicable to the class of piecewise smooth conductivities. This class is important since it describes the conductivity distribution in the human body, as well as those arising in process tomography, such as stratified media in a pipeline. The 2-D case considered here is applicable to reconstruction of a cross-section of a pipeline or a human chest, for example.

The mathematical model of EIT is the inverse conductivity problem of Calderón [10]. We restrict our discussion here to the following two-dimensional setting. Let $\Omega \subset \mathbb{R}^2$ be the unit disc and let $\sigma : \Omega \to (0, \infty)$ be an essentially bounded measurable function satisfying $\sigma(x) \geq c > 0$ for almost every $x \in \Omega$. Let $u \in H^1(\Omega)$ be the unique solution to

$$\nabla \cdot \sigma \nabla u = 0 \text{ in } \Omega, \tag{1.1}$$

$$u\big|_{\partial\Omega} = \phi \in H^{1/2}(\partial\Omega). \tag{1.2}$$

The inverse conductivity problem is to recover σ from the voltage-to-current density map

$$\Lambda_\sigma : \phi \mapsto \sigma \frac{\partial u}{\partial \nu}\Big|_{\partial\Omega},$$

also called the Dirichlet-to-Neumann (DN) map. Here ν is the unit outer normal to the boundary.

Our reconstruction method is based on unique complex geometric optics (CGO) solutions u_1 and u_2 of the conductivity equations

$$\nabla \cdot \sigma \nabla u_1(\,\cdot\,, k) = 0, \qquad \nabla \cdot \sigma^{-1} \nabla u_2(\,\cdot\,, k) = 0, \tag{1.3}$$

where k is a complex parameter and the solutions have asymptotic behaviour $u_1 \sim e^{ikz}$ and $u_2 \sim ie^{ikz}$ when $|z| \to \infty$. To define these global solutions we have set $\sigma(z) \equiv 1$ outside Ω. In particular, this makes the CGO solutions harmonic in $\mathbb{R}^2 \setminus \Omega$. The exponential behaviour of the CGO solutions is used for constructing a nonlinear Fourier analysis for the inverse conductivity problem, and k can be thought of as a frequency-domain variable.

The reconstruction procedure consists of these three steps:

(i) **Recover traces of CGO solutions at the boundary $\partial\Omega$ from the DN map by solving the boundary integral equation given in [2].** The exponential ill-posedness of the EIT problem shows up in this step. We present a new regularized real-linear solution method for the integral equation. The effect of measurement noise is abated by restricting the computation to the disc $|k| < R$, where the truncation radius $R > 0$ depends on the measurement noise level (smaller noise allows the use of larger R). In analogy to linear Fourier transform terminology, we will call R the *low-pass cutoff frequency*.

(ii) **Compute approximate values of CGO solutions inside the unit disc using the *low-pass transport matrix*.** Being harmonic outside Ω, the CGO solutions are determined in $\mathbb{R}^2 \setminus \overline{\Omega}$ by their traces at the boundary $\partial\Omega$. Furthermore, the values of the CGO solutions inside Ω are connected to their values outside Ω through certain Beltrami equations that form a 2×2 linear system. The coefficient matrix for that system on the disk $|k| < R$ is referred to as the low-pass transport matrix.

(iii) **Reconstruct the conductivity.** The approximate conductivity is computed from the recovered values of the CGO solutions inside Ω using differentiation and simple algebra. Numerical implementation of the derivatives is stable due to smoothing provided by the nonlinear low-pass filtering in Step (ii) above.

We remark that there is no smoothness or continuity assumption on the conductivity, and the method solves the full nonlinear EIT problem in an explicitly regularized fashion directly with no iterations. Further, reconstruction at a given point $z \in \Omega$ is independent from the reconstruction at any other point, enabling region-of-interest imaging and trivial parallelization of the algorithm.

Computationally the most demanding part of the reconstruction method is the evaluation of the low-pass transport matrix in Step (ii). The Beltrami equation solver introduced in [3] could be modified and used here but it is rather slow. The computation time can be significantly reduced, and acceptable computation times achieved, using the fast Beltrami equation solver introduced in [17]. We note that numerical solution of Beltrami equations is discussed also in [16, 14], but with asymptotic conditions not suitable for the present work.

For simplicity we restrict here to the special case of Ω being the unit disc, but this is not a serious loss of generality. The method can be modified to apply to any simply connected plane domain with Lipschitz boundary.

In dimension 2, several other algorithms using CGO solutions have preceded the method presented here. The constructive proof for the unique identifiability of isotropic conductivities from infinite-precision data for twice differentiable conductivities [30] led to the first numerical D-bar algorithm [32]. That D-bar algorithm has been applied to simulated data in [23, 27, 28, 33, 34] and to laboratory and *in vivo* human data in [18, 19, 29, 15], resulting in useful reconstructions of both smooth and piecewise smooth conductivities. While the initial scattering transform was regularized using a Born approximation, a more recent paper [24] contains a full nonlinear regularization analysis, including estimates on speed of convergence in Banach spaces, for twice differentiable conductivities. The uniqueness proof for once-differentiable conductivities was provided in [9], and a reconstruction method based on this work is given in [20, 21, 26]. Also, Calderón's original linearized method made use of CGO solutions and has been applied to experimental data in dimension two in [6]. Stability estimates for the reconstruction approach used in this work appeared in [5, 12]. For information about direct algorithms in dimension 3, the reader is referred to [7] and the references therein.

The methods described in the preceding paragraph are all direct methods and permit region-of-interest imaging and parallelization. In addition to these advantages common to the direct algorithms above, the algorithm presented here has the potential for even greater accuracy with respect to magnitude and spatial resolution due to the removal of smoothness assumptions inherent to algorithms based on [30] and [9] or the linearization in [10]. This D-bar algorithm is structured differently

from its predecessors, the main difference being in the use of the low-pass transport matrix to determine the values of the CGO solutions inside Ω from their value outside.

The paper is organized as follows. The CGO solutions are defined in Section 2. The first step in the algorithm is to compute traces of these solutions on $\partial\Omega$ from the Dirichlet-to-Neumann map. The simulation of this map for ideal and noisy data is found in Section 3 and the computation of the traces of the CGO solutions is explained in Section 4.1. The low-pass transport matrix allows us to compute the CGO solutions inside the unit disk from their traces. This step is described in Section 4.2. The reconstruction formula for the conductivity σ is a simple formula given in terms of the CGO solutions inside the unit disk and is also found in Section 4.2. The computational method for solving the Beltrami equations used in the computation of the transport matrix is detailed in Section 5. The results of the numerical tests are found in Section 6. Finally, we conclude our results in Section 7.

2. **Complex geometrical optics solutions.** To construct the CGO solutions (1.3), we first define a real-valued function $\mu : \Omega \to (-1, 1)$ by

$$\mu := \frac{1-\sigma}{1+\sigma}. \tag{2.1}$$

We then consider the complex geometrical optics (CGO) solutions $f_\mu = f_\mu(z,k)$ of the Beltrami equation

$$\overline{\partial}_z f_\mu = \mu\overline{\partial_z f_\mu}, \tag{2.2}$$

where the solutions can be written in the form

$$f_\mu(z,k) = e^{ikz} M_\mu(z,k), \tag{2.3}$$

and the functions M_μ have the special asymptotics

$$M_\mu(z,k) = \left(1 + \mathcal{O}\left(\frac{1}{z}\right)\right) \text{ as } |z| \to \infty. \tag{2.4}$$

Here k is a complex parameter. Existence, uniqueness and properties of the CGO solutions are discussed in [1]. Note, however, the key relations for a complex function $f = u + iv$,

$$\overline{\partial}_z f_\mu = \mu\overline{\partial_z f_\mu} \quad \Leftrightarrow \quad \nabla\cdot\sigma\nabla u = 0 \text{ and } \nabla\cdot\sigma^{-1}\nabla v = 0,$$

connecting the PDE's (1.1) and (2.2).

Set

$$h_+ = \frac{1}{2}(f_\mu + f_{-\mu}), \qquad h_- = \frac{i}{2}(\overline{f_\mu} - \overline{f_{-\mu}}). \tag{2.5}$$

Then the functions $u_1(z,k)$ and $u_2(z,k)$ in formula (1.3) are given by

$$u_1 = h_+ - ih_-, \qquad u_2 = i(h_+ + ih_-). \tag{2.6}$$

An important special feature of the CGO solutions $u_j(z,k)$ is that in the frequency domain they satisfy the equation

$$\overline{\partial}_k u_j(z,k) = -i\,\tau_\sigma(k)\,\overline{u_j(z,k)}, \qquad j = 1,2, \tag{2.7}$$

where the coefficient $\tau_\sigma(k)$ does *not* depend on the space variable. For details see [4, Corollary 18.4.4] or [1, Theorem 5.5].

3. **Simulation of boundary data.** Denote by $\widetilde{H}^s(\partial\Omega)$ the space of $H^s(\partial\Omega)$ functions having mean value zero. For arbitrary $g \in \widetilde{H}^{-1/2}(\partial\Omega)$, let $u \in H^1(\Omega)$ be the solution of the Neumann problem

$$\nabla \cdot \sigma \nabla u = 0 \text{ in } \Omega, \qquad \sigma \frac{\partial u}{\partial \nu} = g \text{ on } \partial\Omega. \tag{3.1}$$

The solution to (3.1) is unique only up to a constant, but the additional requirement $\int_{\partial\Omega} u\, ds = 0$ fixes the solution uniquely. The Neumann-to-Dirichlet (ND) map $\mathcal{R}_\sigma : \widetilde{H}^{-1/2}(\partial\Omega) \to \widetilde{H}^{1/2}(\partial\Omega)$ is now defined by $\mathcal{R}_\sigma g = u|_{\partial\Omega}$.

We note two key equalities connecting the DN map Λ_σ and the ND map $\mathcal{R}_\sigma$. Define an averaging operator

$$\mathcal{L}\phi := |\partial\Omega|^{-1} \int_{\partial\Omega} \phi\, ds.$$

From the definitions of Λ_σ and $\mathcal{R}_\sigma$ we see that

$$\Lambda_\sigma \mathcal{R}_\sigma = I \qquad : \widetilde{H}^{-1/2}(\partial\Omega) \to \widetilde{H}^{-1/2}(\partial\Omega), \tag{3.2}$$

$$\mathcal{R}_\sigma \Lambda_\sigma = I - \mathcal{L} \qquad : H^{1/2}(\partial\Omega) \to \widetilde{H}^{1/2}(\partial\Omega). \tag{3.3}$$

In the above we used the fact that for any $f \in H^{1/2}(\partial\Omega)$ we have

$$\mathcal{L}\Lambda_\sigma f = |\partial\Omega|^{-1} \int_{\partial\Omega} \sigma \frac{\partial u}{\partial \nu}\, ds = |\partial\Omega|^{-1} \int_\Omega \nabla \cdot \sigma \nabla u = 0.$$

Parameterizing the boundary of our domain by θ, the applied current density $g(\theta)$ must have the property that $\int_0^{2\pi} g(\theta) d\theta = 0$. For $n = 1, \ldots, 2N$, define a set of trigonometric basis functions:

$$\phi_n(\theta) = \begin{cases} \pi^{-1/2} \cos\left(\dfrac{(n+1)\theta}{2}\right), & \text{for odd } n, \\ \\ \pi^{-1/2} \sin\left(\dfrac{n\theta}{2}\right), & \text{for even } n. \end{cases} \tag{3.4}$$

Any function $g \in L^2(\partial\Omega)$ representing current density on the boundary can then be approximated by

$$g(\theta) \approx \sum_{n=1}^{2N} \langle g, \phi_n \rangle\, \phi_n(\theta), \tag{3.5}$$

where the inner product is defined for real-valued functions $f, g \in L^2(\partial\Omega)$ by

$$\langle f, g \rangle := \int_0^{2\pi} f(\theta) g(\theta)\, d\theta. \tag{3.6}$$

Given a linear operator $\mathcal{A} : L^2(\partial\Omega) \to L^2(\partial\Omega)$, define its matrix approximation $A \in \mathbb{R}^{2N \times 2N}$ by setting $A := [A_{mn}]$ with

$$A_{mn} := \langle \mathcal{A}\phi_n, \phi_m \rangle. \tag{3.7}$$

Here $m \in \{1, \ldots, 2N\}$ is the row index and $n \in \{1, \ldots, 2N\}$ is the column index. Now define the $2N \times 2N$ matrix approximation $[R_{mn}]$ to the ND map by

$$R_{mn} = \langle u_n|_{\partial\Omega}, \phi_m \rangle \tag{3.8}$$

where $u_n|_{\partial\Omega}$ is the solution to (3.1) with $g = \phi_n$.

We simulate EIT measurements by constructing the matrix $[R_{mn}]$ numerically by repeatedly solving (3.1) using the finite element method (FEM), see [35]. We

compute the inner products (3.8) using a quadrature rule and determine a matrix approximation for the DN map using the identities (3.2) and (3.3). In practice one typically measures a finite-precision discrete current-to-voltage map. That is, known currents are applied on the electrodes, and the resulting voltage is measured with finite precision (and noise). Currents are applied instead of voltages because of advantages in the signal-to-noise ratio.

Note that here we are using a continuous electrode model since we are not modeling electrode effects in our FEM solution of the forward problem.

Define $\widetilde{L}_\sigma$ as the following matrix of size $2N \times 2N$:

$$\widetilde{L}_\sigma := [R_{mn}]^{-1};$$

We add simulated measurement noise by defining a $2N \times 2N$ matrix E with entries of random numbers independently distributed according to a Gaussian normal density $N(0,1)$. The matrix $\widetilde{L}_\sigma$ is then perturbed so that $\widetilde{L}'_\sigma = \widetilde{L}_\sigma + cE$ where $c > 0$ is a constant that is adjusted to obtain the desired relative noise level. Since the DN map is self-adjoint, we then define the noisy map L_σ by

$$L_\sigma = \frac{1}{2}(\widetilde{L}'_\sigma + (\widetilde{L}'_\sigma)^T), \tag{3.9}$$

and the relative noise level by

$$\frac{\|\widetilde{L}_\sigma - L_\sigma\|_{2,2}}{\|\widetilde{L}_\sigma\|_{2,2}}. \tag{3.10}$$

4. Computational reconstruction method.

4.1. Recovering traces of CGO solutions from the DN map.

The crucial object here is the μ-Hilbert transform $\mathcal{H}_\mu : H^{1/2}(\partial\Omega) \to H^{1/2}(\partial\Omega)$. By definition, $v = \mathcal{H}_\mu(u)$, if $f = u + iv$ satisfies (2.2) and $\int_{\partial\Omega} v\, ds = 0$. Then for real-valued functions $g \in H^{1/2}(\partial\Omega)$ we have the formula

$$\partial_T \mathcal{H}_\mu g = \Lambda_\sigma g. \tag{4.1}$$

Here ∂_T is the tangential derivative along the boundary; it can be approximated in the basis (3.4) by the $2N \times 2N$ matrix D_T defined by

$$D_T = \begin{bmatrix} 0 & 1 & & & & & & \\ -1 & 0 & & & & & & \\ & & 0 & 2 & & & & \\ & & -2 & 0 & & & & \\ & & & & \ddots & & & \\ & & & & & & 0 & N \\ & & & & & & -N & 0 \end{bmatrix}. \tag{4.2}$$

By equations (3.9) and (4.1) and (4.2) we can approximate $\mathcal{H}_\mu$ acting on real-valued, zero-mean functions expanded in the basis (3.4) by

$$\widetilde{H}_\mu := D_T^{-1} L_\sigma. \tag{4.3}$$

In general, the traces of the CGO solutions at $\partial\Omega$ do not have mean zero, and so we append the basis function $\phi_0 = (2\pi)^{-1/2}$ to (3.4). This leads to the following $(2N+1) \times (2N+1)$ matrix approximation to the μ-Hilbert transform $\mathcal{H}_\mu$:

$$H_\mu := \begin{bmatrix} 0 & 0 \\ 0 & \widetilde{H}_\mu \end{bmatrix}. \tag{4.4}$$

Furthermore, we can approximate $\mathcal{H}_{-\mu}$ when we have H_μ available. We have the identity

$$\mathcal{H}_\mu \circ (-\mathcal{H}_{-\mu})u = (-\mathcal{H}_{-\mu}) \circ \mathcal{H}_\mu u = u - \mathcal{L}u, \tag{4.5}$$

so $-\mathcal{H}_{-\mu}$ is the inverse operator of $\mathcal{H}_\mu$ in the subspace of zero-mean functions. Thus we may define a $(2N+1) \times (2N+1)$ matrix approximation to $\mathcal{H}_{-\mu}$:

$$H_{-\mu} := \begin{bmatrix} 0 & 0 \\ 0 & -\widetilde{H}_\mu^{-1} \end{bmatrix}. \tag{4.6}$$

Summarizing, once we have measured the DN matrix (3.9), we can approximate the μ-Hilbert transforms $\mathcal{H}_{\pm\mu}$ by matrices $H_{\pm\mu}$ acting on the basis (3.4) augmented by a constant basis function.

However, so far we can only work with *real-valued* functions in $H^{1/2}(\partial\Omega)$, and the CGO solutions are in general complex-valued. Furthermore, the operator $\mathcal{H}_\mu$ is not complex-linear but only real-linear: for a real-valued function g we have

$$\mathcal{H}_\mu(ig) = i\mathcal{H}_{-\mu}(g). \tag{4.7}$$

We represent complex-valued functions $g \in H^{1/2}(\partial\Omega)$ by expanding the real and imaginary parts separately and organizing the coefficients as the following vertical vector in $\mathbb{R}^{4N+2}$:

$$[\langle \operatorname{Re} g, \phi_0\rangle, \langle \operatorname{Re} g, \phi_1\rangle, \dots, \langle \operatorname{Re} g, \phi_{2N}\rangle, \langle \operatorname{Im} g, \phi_0\rangle, \langle \operatorname{Im} g, \phi_1\rangle, \dots, \langle \operatorname{Im} g, \phi_{2N}\rangle]^T.$$

Now the μ-Hilbert transforms $\mathcal{H}_{\pm\mu}$ can be approximated using the following $(4N+2) \times (4N+2)$ matrices:

$$\mathcal{H}_\mu \approx \begin{bmatrix} H_\mu & 0 \\ 0 & H_{-\mu} \end{bmatrix}, \qquad \mathcal{H}_{-\mu} \approx \begin{bmatrix} H_{-\mu} & 0 \\ 0 & H_\mu \end{bmatrix}, \tag{4.8}$$

where H_μ and $H_{-\mu}$ are given by (4.4) and (4.6), respectively.

The infinite-precision boundary integral equation is defined as follows. In analogy with the Riesz projections we define the real-linear operator $\mathcal{P}_\mu : H^{1/2}(\partial\mathbb{D}) \to H^{1/2}(\partial\mathbb{D})$ by the formula

$$\mathcal{P}_\mu g = \frac{1}{2}(I + i\mathcal{H}_\mu)g + \frac{1}{2}\mathcal{L}g, \tag{4.9}$$

where the function g may be complex-valued. Further, denote

$$\mathcal{P}_\mu^k := e^{-ikz}\mathcal{P}_\mu e^{ikz}, \tag{4.10}$$

containing complex-linear operators of point-wise multiplication by exponential functions. Matrices for such a multiplication operator (for fixed k) can be constructed quite simply by applying it numerically to each basis function and computing inner products between the result and each basis function.

It was shown in [2] that the following boundary integral equation holds:

$$M_\mu(\cdot\,, k)|_{\partial\mathbb{D}} + 1 = (\mathcal{P}_\mu^k + \mathcal{P}_0)M_\mu(\cdot\,, k)|_{\partial\mathbb{D}}, \tag{4.11}$$

where the function M_μ is as in (2.3). We can thus solve (4.11) for the trace of $M_\mu(\cdot\,, k)$ on $\partial\Omega$ and use (2.3) to find the trace of $f_\mu(\cdot\,, k)$ as well.

Numerical solution of (4.11) is done by writing real and imaginary parts separately, replacing all the operators by their $(4N+2)\times(4N+2)$ matrix approximations, and solving the resulting finite linear system in a regularized manner.

Because of the conjugation with exponential functions in (4.10), the error in H_μ gets multiplied with numbers exponentially large in k, and so we can only

reliably numerically solve the boundary integral equation (4.11) for k ranging in a disc $D(0,R)$ where the radius $R>0$ depends on the noise level. This is where the exponential ill-posedness of the inverse conductivity problem shows up in our reconstruction method. We regularize the reconstruction by truncation of coefficient functions to the disc $|k|<R$; in other words replacing the function values by zero outside that disc.

4.2. **The low-pass transport matrix and conductivity reconstruction.** Suppose we know the trace of the CGO solution $f_\mu(\,\cdot\,,k)$ on $\partial\Omega$. Then we can expand it as a Fourier series at the boundary. Now equation (2.2) and the fact that μ is supported in Ω implies that $f_\mu(\,\cdot\,,k)$ is analytic outside the unit disc. Therefore the coefficients of the Fourier series can be used to expand f_μ as a power series outside Ω. In other words, the trace of $f_\mu(\,\cdot\,,k)$ on $\partial\Omega$ determines f_μ outside Ω in a straightforward way.

Choose then a point $z_0\in\mathbb{R}^2\setminus\overline{\Omega}$. As explained above, we know $f_\mu(z_0,k)$ and $f_{-\mu}(z_0,k)$ for any $|k|<R$. Use (2.5) to construct the function

$$\nu_{z_0}^{(R)}(k):=\begin{cases} i\dfrac{h_-(z_0,k)}{h_+(z_0,k)} & \text{for } |k|<R,\\[2ex] 0 & \text{for } |k|\geq R.\end{cases} \tag{4.12}$$

We next solve the truncated Beltrami equations

$$\overline{\partial}_k\alpha^{(R)} = \nu_{z_0}^{(R)}(k)\,\overline{\partial_k\alpha^{(R)}}, \tag{4.13}$$

$$\overline{\partial}_k\beta^{(R)} = \nu_{z_0}^{(R)}(k)\,\overline{\partial_k\beta^{(R)}}, \tag{4.14}$$

with solutions represented in the form

$$\alpha^{(R)}(z,z_0,k) = \exp(ik(z-z_0)+\varepsilon(k)), \tag{4.15}$$

$$\beta^{(R)}(z,z_0,k) = i\exp(ik(z-z_0)+\widetilde{\varepsilon}(k)), \tag{4.16}$$

where $\varepsilon(k)/k\to 0$ and $\widetilde{\varepsilon}(k)/k\to 0$ as $k\to\infty$. Requiring

$$\alpha^{(R)}(z,z_0,0)=1 \quad\text{and}\quad \beta^{(R)}(z,z_0,0)=i \tag{4.17}$$

fixes the solutions uniquely, see Section 5.1.

Fix any nonzero $k_0\in\mathbb{C}$ and choose any point z inside the unit disc. We can now use the approximate transport matrix

$$T^{(R)}=T^{(R)}_{z,z_0,k_0}:=\begin{pmatrix} a_1^{(R)} & a_2^{(R)}\\ b_1^{(R)} & b_2^{(R)}\end{pmatrix} \tag{4.18}$$

to compute

$$\begin{aligned} u_1^{(R)}(z,k_0) &= a_1^{(R)}u_1(z_0,k_0)+a_2^{(R)}u_2(z_0,k_0),\\ u_2^{(R)}(z,k_0) &= b_1^{(R)}u_1(z_0,k_0)+b_2^{(R)}u_2(z_0,k_0),\end{aligned} \tag{4.19}$$

where $\alpha^{(R)}=a_1^{(R)}+ia_2^{(R)}$ and $\beta^{(R)}=b_1^{(R)}+ib_2^{(R)}$. The truncation in (4.12) can be interpreted as a nonlinear low-pass filter in the k-plane. This is where the term *low-pass transport matrix* originates.

To see the role of equations (4.19) recall that since $u_1(z_0,k_0)$ and $u_2(z_0,k_0)$ are $\mathbb{R}$-linearly independent [4, Theorem 18.4.1], we can always write $u_j(z,k_0)$ as a linear combination of them. However, the key point here is that, e.g. if we write $u_1(z,k_0)=a_1\,u_1(z_0,k_0)+a_2\,u_2(z_0,k_0)$, then a straightforward calculation using the

$\overline{\partial}_k$-equations (2.7) implies that the function $\alpha = a_1 + ia_2$ satisfies equation (4.13) with the untruncated coefficient $\nu_{z_0}(k)$. Furthermore (4.15) holds with $\alpha(z, z_0, 0) = 1$, see [1], and similar argument applies to $\beta(z, z_0, k)$.

Given the above we know the approximate solutions $u_j^{(R)}(z, k_0)$ for $z \in \mathbb{D}$ and one fixed k_0. We use formulas (2.5) and (2.6) to connect $u_1^{(R)}, u_2^{(R)}$ with $f_\mu^{(R)}, f_{-\mu}^{(R)}$. Define

$$\mu^{(R)}(z) = \frac{\overline{\partial} f_\mu^{(R)}(z, k_0)}{\partial \overline{f_\mu^{(R)}}(z, k_0)}. \tag{4.20}$$

Finally we reconstruct the conductivity σ approximatively as

$$\sigma^{(R)} = \frac{1 - \mu^{(R)}}{1 + \mu^{(R)}}. \tag{4.21}$$

5. **Beltrami equation solver.** We now show that the problems (4.13)-(4.16) have unique solutions given the requirement that the transport matrix be the identity at $k = 0$. With the truncation of ν_{z_0} to $\nu_{z_0}^{(R)}$ the sublinear terms $\varepsilon(k)$ and $\widetilde{\varepsilon}(k)$ in (4.15)-(4.16) become analytic outside the disk of radius R (apply here [4, Theorem 5.5.1]), hence bounded and this in turn results in $\mathbb{R}$-linear equations for which numerical solvers were studied in [3, 17].

Below, we keep the variable z fixed.

5.1. **Constructing the low-pass transport matrix.** Assume $2 < p < 1 + 1/q$, where q is a constant such that $|\nu_{z_0}^{(R)}(k)| \leq q < 1$ for all $k \in \mathbb{C}$ [1, Proposition 6.3]. To construct the truncated transport matrix (4.18), first find solutions η_1, $\eta_2 \in W^{1,p}_{\mathrm{loc}}(\mathbb{R}^2)$ to the equation

$$\overline{\partial}_k \eta = \nu_{z_0}^{(R)}(k)\, \overline{\partial_k \eta}, \tag{5.1}$$

with asymptotics

$$\eta_1(k) = e^{ik(z-z_0)}\big(1 + \mathcal{O}(1/k)\big) \quad \text{and} \quad \eta_2(k) = i\, e^{ik(z-z_0)}\big(1 + \mathcal{O}(1/k)\big), \tag{5.2}$$

respectively, as $|k| \to \infty$. Such solutions exist and are unique by [1, Theorem 4.2]. In fact, we are here constructing CGO solutions, but now in the frequency domain.

The solutions are complex valued, but pointwise $\mathbb{R}$-linearly independent by [4, Theorem 18.4.1]. Hence there are constants $A, B \in \mathbb{R}$ such that

$$A\, \eta_1(0) + B\, \eta_2(0) = 1.$$

We now set

$$\alpha^{(R)}(z, z_0, k) = A\, \eta_1(k) + B\, \eta_2(k), \qquad k \in \mathbb{R}^2.$$

Then $\alpha^{(R)}(z, z_0, k)$ satisfies (4.13) and the first condition in (4.17). Applying [1, Corollary 3.4] to $F(k) := e^{-ik(z-z_0)}\alpha^{(R)}(z, z_0, k)$ gives

$$F(k) = \exp\left(C_0 + \varepsilon(k)\right), \qquad C_0 \text{ a constant and } \varepsilon(k) \to 0 \text{ as } k \to \infty.$$

Thus we have the required asymptotics (4.15), completing the construction of $\alpha^{(R)}(z, z_0, k)$. Applying similarly [1, Corollary 3.4] to the difference of two solutions to (4.13), (4.15) shows that if the solutions agree at one point, then they are identical. Hence we have also the uniqueness of the function $\alpha^{(R)}(z, z_0, k)$. The same argument with [1, Corollary 3.4] also shows that at every k, the function values $\alpha^{(R)}(z, z_0, k)$, $\beta^{(R)}(z, z_0, k)$ are $\mathbb{R}$-linearly independent. Thus the low-pass transport matrices are invertible at every point.

5.2. **Solving $\mathbb{R}$-linear Beltrami equations.** To solve the equation (5.1) with either of the asymptotics in (5.2) we argue as in [1]. Making the substitution $\eta(k) = e^{ik(z-z_0)}\big(1+\omega(k)\big)$ we obtain the $\mathbb{R}$-linear equation

$$\overline{\partial}_k\omega + \gamma_1\overline{\partial_k\omega} + \gamma_2\overline{\omega} + \gamma_2 = 0 \tag{5.3}$$

with the asymptotic condition $\lim_{k\to\infty}\omega(k) = 0$, where

$$\gamma_1(z,z_0,k) = \pm\, e_{-(z-z_0)}(k)\,\nu_{z_0}^{(R)}(k), \tag{5.4}$$

$$\gamma_2(z,z_0,k) = -i\,(\overline{z-z_0})\,\gamma_1(z,z_0,k), \tag{5.5}$$

with $e_z(k) = e^{i(kz+\overline{k}\overline{z})}$. We solve numerically this equation as described in [17].

Substitute $u \in L^p(D(0,R))$ such that $\overline{u} = -\overline{\partial}_k\omega$. Then $\omega = -P\overline{u}$ and $\partial_k\omega = -S\overline{u}$, where P is the solid Cauchy transform and S is the Beurling transform defined by

$$Pf(z) = -\frac{1}{\pi}\int_{\mathbb{C}}\frac{f(\lambda)}{\lambda - z}dm(\lambda), \qquad Sg(z) = -\frac{1}{\pi}\int_{\mathbb{C}}\frac{g(\lambda)}{(\lambda-z)^2}dm(\lambda),$$

where the latter is a principal value integral, the points $(\lambda_1,\lambda_2)\in\mathbb{R}^2$ and $\lambda_1+i\lambda_2\in\mathbb{C}$ are identified, and dm denotes Lebesgue measure in $\mathbb{R}^2$. This leads to the $\mathbb{R}$-linear integral equation

$$u + (\overline{\gamma_1}S + \overline{\gamma_2}P)\overline{u} = \overline{\gamma_2}. \tag{5.6}$$

5.3. **Discretization.** We form a uniform grid in $[-R,R]^2$ allowing the use of fast Fourier transform (FFT) for matrix-vector products. Choose a positive integer m, let $N = 2^m$, $h = 2R/N$ and define

$$\mathbb{Z}_N^2 = \big\{(j_1,j_2)\in\mathbb{Z}^2 \,\big|\, -N/2 \le j_1, j_2 < N/2\big\}. \tag{5.7}$$

The uniform grid consists of the points $\big\{jh \,\big|\, j\in\mathbb{Z}_N^2\big\}$.

The grid approximation of a function $v : [-R,R]^2 \to \mathbb{C}$ is defined by $v_h : \mathbb{Z}_N^2 \to \mathbb{C}$ with $v_h(j) := v(jh)$. The Cauchy transform Pv and the Beurling transform Sv are discretized by

$$(P_hv_h)(j) = \frac{1}{\pi h}\sum_{\substack{l\neq j\\ l\in\mathbb{Z}_N^2}}\frac{1}{j-l}v_h(l), \qquad (S_hv_h)(j) = -\frac{1}{\pi}\sum_{\substack{l\neq j\\ l\in\mathbb{Z}_N^2}}\frac{1}{(j-l)^2}v_h(l),$$

where $(Pv)(jh) \approx (P_hv_h)(j)$ and $(Sv)(jh)\approx(S_hv_h)(j)$ for $j\in\mathbb{Z}_N^2$. The Toeplitz structure of these discretizations allows fast computation of the products P_hv_h and S_hv_h by executing the FFT.

The functions $\gamma_i \quad (i=1,2)$ are discretized by

$$\gamma_{i,h}(j) = \gamma_i(z,z_0,jh).$$

Finally, we obtain the discretized form of (5.6) as

$$u_h + (\overline{\gamma_{1,h}}S_h + \overline{\gamma_{2,h}}P_h)\overline{u_h} = \overline{\gamma_{2,h}} \tag{5.8}$$

and $\omega_h = -P_h\overline{u_h}$ is an approximate solution to (5.3). To solve this equation, we execute the iterative generalized minimal residual (GMRES) method [31] by using a preconditioner we describe next.

We make a substitution to (5.8) having a two-fold advantage. Let $A_h = \overline{\gamma_{1,h}}S_h + \overline{\gamma_{2,h}}P_h$ and substitute $u_h = w_h - A_h\overline{w_h}$. We then get a $\mathbb{C}$-linear equation

$$(I - A_h\overline{A_h})w_h = \overline{\gamma_{2,h}}, \tag{5.9}$$

where $\overline{A_h} w_h = \overline{A_h \overline{w_h}}$. This preconditioning resulted in the fastest convergence of GMRES for the equation (5.8) in comparison to the other options considered in [17].

The second advantage of this substitution comes from the requirement of having to solve two Beltrami equations of type (5.3) for each z-point as described in Section 5.1. Let us denote the functions and operators corresponding to the first equation by $\gamma^+_{i,h}$ $(i = 1, 2)$ and A^+_h, and those of the second equation by $\gamma^-_{i,h}$ and A^-_h. We notice that $\gamma^-_i = -\gamma^+_i$. Therefore $A^-_h = -A^+_h$ as well, resulting in $I - A^+_h \overline{A^+_h} = I - A^-_h \overline{A^-_h}$. Hence, to solve the two equations

$$(I - A^+_h \overline{A^+_h}) w^+_h = \overline{\gamma^+_{2,h}},$$
$$(I - A^-_h \overline{A^-_h}) w^-_h = \overline{\gamma^-_{2,h}}$$

we merely solve the first one and then set $w^-_h = -w^+_h$.

6. **Numerical results.** Four example conductivities are studied: a simple heart-and-lungs phantom σ_1 related to monitoring intensive care patients, similar heart-and-lungs phantoms σ_2 and σ_3 both featuring a low-conductivity spine, and σ_2 an additional tumor-like inhomogeneity inside one of the lungs. The fourth example is a conductivity cross-section σ_4 of a stratified medium that could arise, for example, in an oil pipeline or other industrial process monitoring applications.

All these conductivities are discontinuous and therefore violate the assumptions of previously published D-bar reconstruction methods.

6.1. **Heart-and-lungs phantom.** We define an idealized computational model of a cross-section of a patient's chest, see the leftmost image in Figure 2. The conductivity values are

Background	1.0,
Lung (blue)	0.7,
Heart (red)	2.0.

We simulate boundary measurements using FEM to solve equation (3.1). We let n range from 1 to 32, so $N = 16$. This choice corresponds approximately to an EIT configuration with 32 equispaced electrodes located on the unit circle. Our FEM mesh comprises 263 169 nodes and 524 288 triangles. For a numerical test comparing analytically and numerically computed ND maps for the constant conductivity $\sigma \equiv 1$, our computed ND matrix elements have at least 5 correct digits. We then add 0.01% noise using (3.9), which is the published noise level of the 32-electrode ACT3 system of Rensselaer Polytechnic Institute [13]. We remark that since EIT is exponentially ill-posed, this seemingly low noise level is significant.

We solve the matrix version of the boundary integral equation (4.11) for the traces of CGO solutions with k ranging in a finite grid inside the disc $|k| < R$. Regularization is implemented using the Moore-Penrose pseudoinverse. The cutoff frequency R is taken as large as possible without too much numerical error, resulting in $R = 6$ for the data with no added noise and $R = 5.5$ for the data with 0.01% noise. More advanced or automatic choices of R are not discussed in this work. Truncation is used in the algorithms based on [30] and [9] as well, and the reader is referred to [24] for a study of truncation as a regularization method for the D-bar algorithm based on [30].

We choose $z_0 = 1.4$ and use (4.12) to evaluate the function $\nu^{(R)}_{z_0}(k)$ numerically in the disc $|k| < R$. Plot of ν_{z_0} with $R = 6$ is shown in Figure 1. Further, we choose the point k_0 in Section 4.2 as the nearest k-grid point to 1.

We construct a finite Cartesian grid of points in the unit disc, and for each of those points $z \in \Omega$ the truncated Beltrami equation (4.13) for $\alpha^{(R)}$ is solved using the quasilinear asymptotic condition (4.15) depending on z. Substituting the result into (4.20) and (4.21) yields an approximate reconstruction of the conductivity at z. Numerical differentiation in (4.20) is not problematic as the low-pass filtering results in smooth functions to be differentiated.

Figure 2 shows the two reconstructions together with relative errors given by

$$\frac{\|\sigma - \sigma^{(R)}\|_{L^2(\Omega)}}{\|\sigma\|_{L^2(\Omega)}} \cdot 100\%. \tag{6.1}$$

The relative errors of the reconstructions are 11.6% and 12.7%.

Further, we define the dynamic range of a reconstruction to be 100% multiplied by the ratio of the difference of the maximum and minimum values in the reconstruction to the difference of maximum and minimum values of the true conductivity. The minimum conductivity in the noise-free reconstruction is 0.637 (compared to a true value of 0.7), and the maximum conductivity is 1.997 (compared to a true value of 2). This results in a dynamic range of 105%. The minimum conductivity in the reconstruction from data with 0.01% noise is 0.637 and the maximum 1.870, resulting in a dynamic range of 95%.

The reconstructions display a high degree of spatial accuracy and lack of artifacts. Notably, the separation between the lungs is clearly visible and the organs are not distorted toward the boundary of the domain.

We remark that different choices for z_0 and k_0 result in slightly differing numerical values in the reconstruction, but we do not discuss such effects further here (with the exception of using several z_0 values in Subsection 6.3).

6.2. **Heart-and-lungs phantom with tumor.** We define another model σ_2 of a cross-section of a patient's chest but now with a resistive spine and a conductive "tumor" in the right lung. The conductivity σ_3 is the same as σ_2 but without the tumor, see Figure 3. The conductivity values are

Background	1.0,
Lung (light blue)	0.7,
Spine (dark blue)	0.2,
Heart (red)	2.0,
Tumor (red)	2.0.

We compute reconstructions from data with no added noise using $R = 5.5$ and otherwise the same parameters as in Subsection 6.1, see Figure 3. Relative errors in the reconstructions of of σ_2 and σ_3 are 16.7% and 16.3% and the dynamic ranges are 109% and 106%, respectively. The latter are computed using the differences between the heart and spine since the maximum and minimum conductivity values occur there.

While the heart, lungs, and spine are all clearly visible, the spine appears somewhat enlarged in the reconstructions, and the separation between the lungs and spine is not as marked as the separation between other organs.

The conductivity of the tumor is 2, the same as that of the heart. However, while the presence of the tumor is evident in the reconstructed image as a region of brighter blue in the lung, its actual conductivity value is not well-reconstructed. A difference image is also included in Figure 3 in which the reconstruction without the tumor is subtracted from the reconstruction with the tumor. In the difference

image, the tumor is strikingly visible, but we note that it is plotted on its own scale, not relative to the plots above. The true contrast in the difference image is 1.3, while the contrast achieved in the difference image is 0.2073.

6.3. **Stratified medium.** The conductivity σ_4 consists of horizontal layers as shown in the bottom left image in Figure 4. The conductivity values are

Top layer	1.2,
Middle layer	2.0,
Bottom layer	0.3.

Such a conductivity could be a rough model of a cross-section of an oil pipeline with sand in the bottom, water in the middle, and oil on top.

Unlike the previous examples, the conductivity σ_4 is not constant near the boundary. This violates the assumptions of the proposed method, and we take this into account as follows. The cross-section of the pipeline is modeled by the disc $|x| \leq 0.7$, and we define $\sigma_3(x) \equiv 1$ for $0.7 < |x| \leq 1$. In principle one could measure EIT data at the boundary $|x| = 0.7$ of the pipeline and determine the DN map on $|x| = 1$ as explained for infinite-precision data in [30, Section 6] and numerically implemented for noisy data in [34]. However, we take the simpler approach of adding the layer around the boundary $0.7 < |x| \leq 1$ in which $\sigma_3 = 1$ and simulating the DN map on $|x| = 1$.

We compute the function ν_{z_0} with $R = 4$ and $z_0 = 1.4$, see Figure 1. The truncation radius is determined visually by increasing it as far as possible before apparent numerical instability. We observe a nonsymmetry in the reconstruction, the highest quality being at the points closest to $z_0 = 1.4$. To obtain a more symmetric reconstruction, we compute four reconstructions $\sigma_E, \sigma_W, \sigma_N, \sigma_S$ computed using $z_0 = 1.4, -1.4, 1.4i, -1.4i$, respectively. Figure 4 shows the combined reconstruction defined by

$$\sigma = .25(1 + z_1)\sigma_E + .25(1 - z_1)\sigma_W + .25(1 + z_2)\sigma_N + .25(1 - z_2)\sigma_S. \tag{6.2}$$

The idea of the weighted sum (6.2) is to emphasize the highest-quality parts of each of the four reconstructions.

The layers are very clearly represented with very few artifacts. One observable artifact is the smoothing that occurs between the layers. However the gradient is quite steep and so it is readily recognized as a layer. The relative error is 24.7% and the dynamic range is 134% inside the disc $|x| < 0.7$.

7. **Discussion and summary.** In this work a new computational EIT algorithm in dimension two is presented, based on the constructive uniqueness proof given by Astala and Päivärinta in [*Ann. of Math.* **163** (2006)]. The method consists of three main steps. First, one must recover traces of CGO solutions from the DN map by solving an ill-posed boundary integral equation introduced in [2]. Second, one approximates the CGO solutions inside the unit disc using a *low-pass transport matrix*. Finally, the approximate conductivity is computed from the CGO solutions inside the unit disc using numerical differentiation and simple algebra.

A fast solver of the Beltrami equation, introduced in [17], was employed to facilitate the computation of the low-pass transport matrix. We stress that although the Beltrami solver is based on the iterative GMRES algorithm, the proposed EIT reconstruction method involves no iterations in the conductivity space.

The method was tested on simulated conductivity distributions with applications in medical imaging and process tomography. The results were very robust with respect to noise in the data and gave a very good representation of the dynamic range of the actual conductivity distribution. The reconstructions are mollified approximations to the discontinuous conductivities, but the gradients are quite steep. Relative errors in the reconstructions are of the same size (or slightly smaller) than similar errors for previous D-bar methods assuming smoothness in the conductivity.

The excellent dynamic range and good spatial resolution indicate that this method holds promise for applications and use with experimental data.

Acknowledgments. This material is based upon work supported by the Finnish Centre of Excellence in Inverse Problems Research (Academy of Finland CoE-project 213476, L. Päivärinta and S. Siltanen) and by the Finnish Center of Excellence in Analysis and Dynamics Research (Academy of Finland projects 1118634 and 118422, K. Astala). The work of S. Siltanen was supported in part by the Computational Science Research Programme of the Academy of Finland (project 134868).

REFERENCES

[1] K. Astala and L. Päivärinta, *Calderón's inverse conductivity problem in the plane*, Ann. of Math. (2), **163** (2006), 265–299.

[2] K. Astala and L. Päivärinta, "A Boundary Integral Equation for Calderón's Inverse Conductivity Problem," Proc. 7th Internat. Conference on Harmonic Analysis, Collectanea Mathematica, 2006.

[3] K. Astala, J. L. Mueller, L. Päivärinta and S. Siltanen, *Numerical computation of complex geometrical optics solutions to the conductivity equation,* Applied and Computational Harmonic Analysis, **29** (2010), 2–17.

[4] K. Astala, T. Iwaniec and G. Martin, "Elliptic Partial Differential Equations and Quasiconformal Mappings in the Plane," Princeton Mathematical Series, **48**, Princeton University Press, Princeton, NJ, 2009.

[5] T. Barceló, D. Faraco, and A. Ruiz. *Stability of calderón inverse conductivity problem in the plane*, Journal de Mathématiques Pures et Appliqués, **88** (2007), 522–556.

[6] J. Bikowski and J. L. Mueller *2D EIT reconstructions using Calderón's method*, Inverse Problems and Imaging, **2** (2008), 43–61.

[7] J. Bikowski, K. Knudsen and J. L. Mueller, *Direct numerical reconstruction of conductivities in three dimensions using scattering transforms,* Inverse Problems, **27** (2011), 19 pp.

[8] G. Boverman, D. Isaacson, T.-J. Kao, G. Saulnier and J. C. Newell, "Methods for Direct Image Reconstruction for EIT in Two and Three Dimensions," Proceedings of the 2008 Electrical Impedance Tomography Conference at Dartmouth College, Hanover, New Hampshire, June 16 to 18, 2008.

[9] R. M. Brown and G. Uhlmann, *Uniqueness in the inverse conductivity problem for nonsmooth conductivities in two dimensions*, Comm. Partial Differential Equations, **22** (1997), 1009–1027.

[10] A. P. Calderón, *On an inverse boundary value problem*, in "Seminar on Numerical Analysis and its Applications to Continuum Physics (Rio de Janeiro, 1980), Soc. Brasileira de Matemàtica, Rio de Janeiro, (1980), 65–73.

[11] M. Cheney, D. Isaacson and J. C. Newell, *Electrical impedance tomography*, SIAM Review, **41** (1999), 85–101.

[12] A. Clop, D. Faraco and A. Ruiz. *Integral stability of calderón inverse conductivity problem in the plane*, Inverse Problems and Imaging, **4** (2010), 49–91.

[13] R. D. Cook, G. J. Saulnier and J. C. Goble "A Phase Sensitive Voltmeter for a High-Speed, High-Precision Electrical Impedance Tomograph," Proc. Annu. Int. Conf. IEEE Engineering in Medicine and Biology Soc., (1991), 22–23.

[14] P. Daripa, *A fast algorithm to solve the Beltrami equation with applications to quasiconformal mappings*, Journal of Computational Physics, **106** (1993), 355–365.

[15] M. DeAngelo and J. L. Mueller, *D-bar reconstructions of human chest and tank data using an improved approximation to the scattering transform,* Physiological Measurement, **31** (2010), 221–232.
[16] D. Gaydashev and D. Khmelev, *On numerical algorithms for the solution of a Beltrami equation*, `arXiv:math/0510516`, 2005.
[17] M. Huhtanen and A. Perämäki, *Numerical solution of the $\mathbb{R}$-linear Beltrami equation*, to appear in Math. Comp.
[18] D. Isaacson, J. L. Mueller, J. C. Newell and S. Siltanen, *Reconstructions of chest phantoms by the D-bar method for electrical impedance tomography*, IEEE Trans. Med. Im., **23** (2004), 821–828.
[19] D. Isaacson, J. L. Mueller, J. C. Newell and S. Siltanen, *Imaging cardiac activity by the D-bar method for electrical impedance tomography*, Physiological Measurement, **27** (2006), S43–S50.
[20] K. Knudsen, "On the Inverse Conductivity Problem," Ph.D. thesis, Department of Mathematical Sciences, Aalborg University, Denmark, 2002.
[21] K. Knudsen, *A new direct method for reconstructing isotropic conductivities in the plane,* Physiol. Meas., **24** (2003), 391–401.
[22] K. Knudsen, M. Lassas, J. L. Mueller and S. Siltanen, "Reconstructions of Piecewise Constant Conductivities by the D-Bar Method for Electrical Impedance Tomography," Proceedings of the 4th AIP International Conference and the 1st Congress of the IPIA, Vancouver, Journal of Physics: Conference Series, **124**, 2008.
[23] K. Knudsen, M. Lassas, J. L. Mueller and S. Siltanen, *D-bar method for electrical impedance tomography with discontinuous conductivities*, SIAM J. Appl. Math., **67** (2007), 893–913.
[24] K. Knudsen, M. Lassas, J. L. Mueller and S. Siltanen, *Regularized D-bar method for the inverse conductivity problem*, Inverse Problems and Imaging, **3** (2009), 599–624.
[25] K. Knudsen, J. L. Mueller and S. Siltanen, *Numerical solution method for the dbar-equation in the plane*, J. Comp. Phys., **198** (2004), 500–517.
[26] K. Knudsen and A. Tamasan, *Reconstruction of less regular conductivities in the plane*, Comm. Partial Differential Equations, **29** (2004), 361–381.
[27] J. L. Mueller and S. Siltanen, *Direct reconstructions of conductivities from boundary measurements*, SIAM J. Sci. Comp., **24** (2003), 1232–1266.
[28] J. L. Mueller, S. Siltanen and D. Isaacson, *A direct reconstruction algorithm for electrical impedance tomography,* IEEE Trans. Med. Im., **21** (2002), 555–559.
[29] E. Murphy, J. L. Mueller and J. C. Newell, *Reconstruction of conductive and insulating targets using the D-bar method on an elliptical domain,* Physiol. Meas., **28** (2007), S101–S114.
[30] A. I. Nachman, *Global uniqueness for a two dimensional inverse boundary value problem*, Ann. of Math. (2), **143** (1996), 71–96.
[31] Y. Saad and M. H. Schultz, *GMRES: A generalized minimal residual algorithm for solving nonsymmetric linear systems*, SIAM J. Sci. Stat. Comput., **7** (1986), 856–869.
[32] S. Siltanen, J. Mueller and D. Isaacson, *An implementation of the reconstruction algorithm of A. Nachman for the 2D inverse conductivity problem,* Inverse Problems, **16** (2000), 681-699, (Erratum: Inverse problems, **17**, 1561–1563).
[33] S. Siltanen, J. Mueller and D. Isaacson, "Reconstruction of High Contrast 2-D Conductivities by the Algorithm of A. Nachman," In "Radon Transforms and Tomography" (South Hadley, MA, 2000), 241–254, Contemporary Mathematics, **278**, Amer. Math. Soc., Providence, RI, 2001.
[34] S. Siltanen and J. Tamminen, *Reconstructing conductivities with boundary corrected D-bar method,* Submitted manuscript.
[35] G. Strang and G. Fix, "An Analysis of The Finite Element Method," Prentice-Hall, Inc., Englewood Cliffs, NJ, 1973.
[36] G. Vainikko, *Fast solvers of the Lippmann-Schwinger equation*, in "Direct and Inverse Problems of Mathematical Physics" (Newark, DE, 1997), 423–440, Int. Soc. Anal. Appl. Comput., **5**, Kluwer Acad. Publ, Dordrecht, 2000.

Received August 2010; revised June 2011.

E-mail address: kari.astala@helsinki.fi;jennifer.l.mueller@gmail.com
E-mail address: ljp@rni.helsinki.fi;allan.peramaki@aalto.fi
E-mail address: samuli.siltanen@helsinki.fi

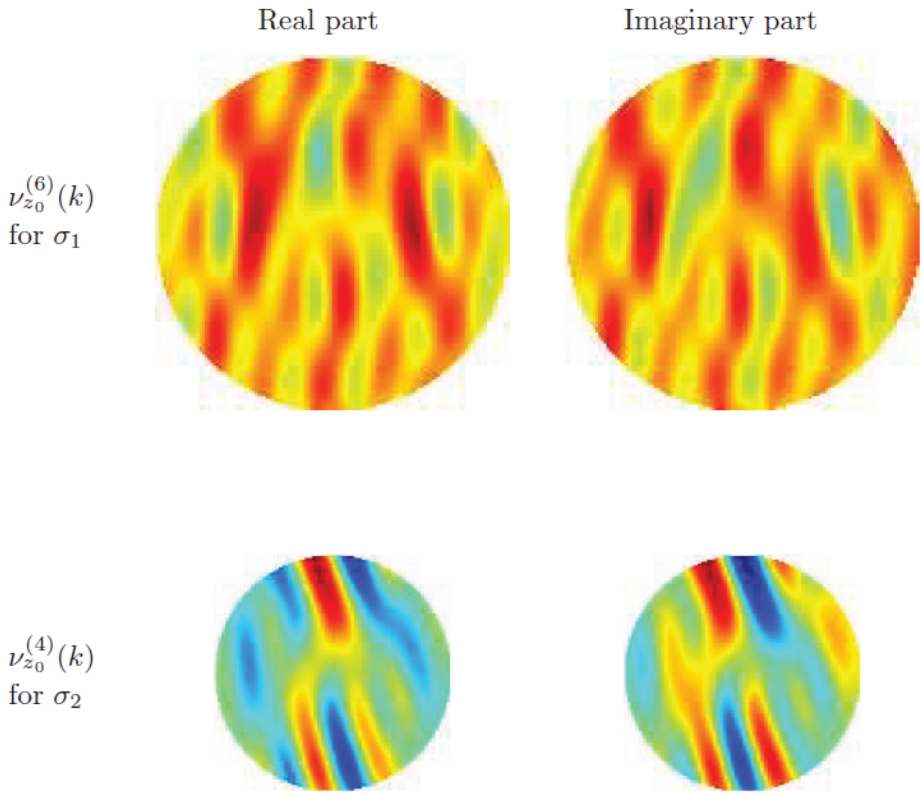

FIGURE 1. Top row: The real (left) and imaginary (right) parts of the function $\nu_{z_0}(k)$ corresponding to the heart-and-lungs phantom σ_1 for $|k| < 6$. Numerical values of the real and imaginary parts range between -0.08 and 0.08. Bottom row: The real (left) and imaginary (right) parts of the function $\nu_{z_0}(k)$ corresponding to the stratified medium conductivity σ_4 (including the added unit conductivity annulus, see Subsection 6.3) for $|k| < 4$. Numerical values of the real and imaginary parts range between -0.25 and 0.26. In both cases $z_0 = 1.4$. The colormaps in all four plots are the same, allowing direct comparison of colors (function values).

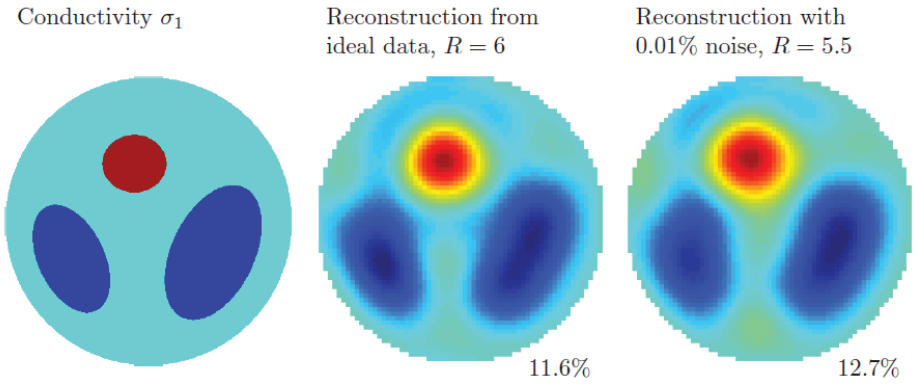

FIGURE 2. Heart-and-lungs conductivity phantom σ_1 and two different reconstructions. The colors (conductivity values) in the three images are directly comparable. The relative error percentages of the two reconstructions are computed using formula (6.1). **Left:** true conductivity σ_1. **Center:** reconstruction from noise-free data with $z_0 = 1.4$ and cutoff frequency $R = 6$. The minimum conductivity in the reconstruction is 0.637 (true value 0.7); the maximum conductivity is 1.997 (true value 2). **Right:** reconstruction from data with added noise of relative size 10^{-4} in the sense of formula (3.10). Here $z_0 = 1.4$ and the cutoff frequency is $R = 5.5$. The minimum conductivity in the reconstruction is 0.637 and the maximum 1.870.

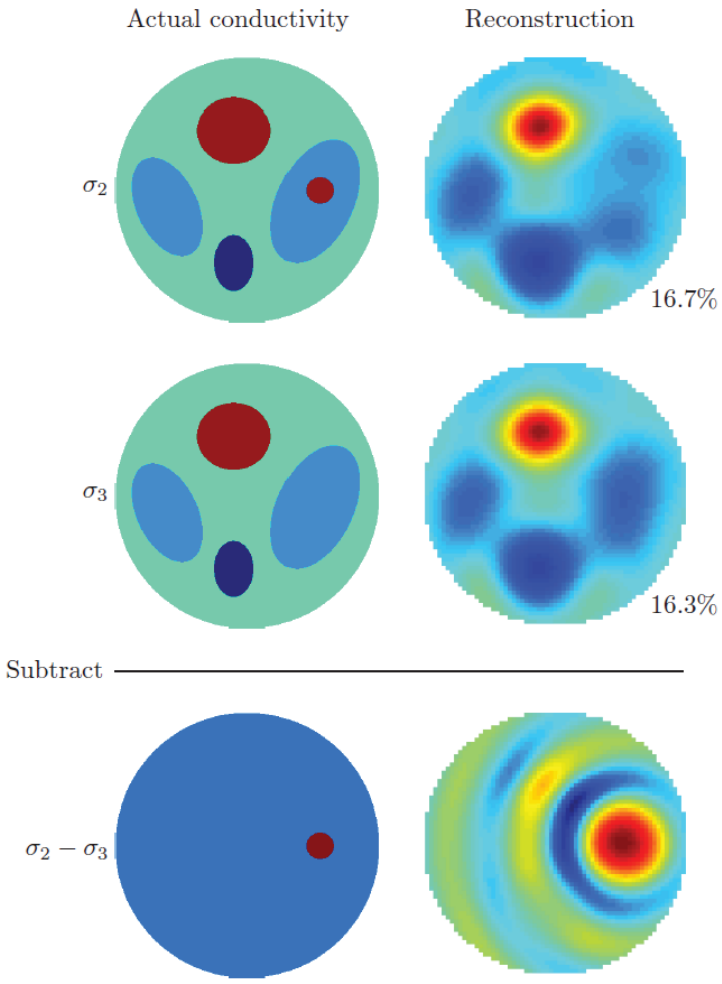

FIGURE 3. True conductivities σ_2 and σ_3 (left) and reconstructions from noise-free data (right). In each case, the cutoff frequency is $R = 5.5$ and $z_0 = 1.4$. The relative error percentages of the two reconstructions are computed using formula (6.1). The bottom row represents a difference image; that is, the reconstruction in the second row is subtracted from the reconstruction in the top row to form the image in the bottom row. In rows 1 and 2, the colormaps in the left and right image are the same. The images in the bottom row are each plotted on their own scale. The true maximum conductivity in the first and second row is 2.0, and the true minimum conductivity is 0.2. The max and min in row one are 2.3319 and 0.3781, respectively. The max and min in row two are 2.2732 and 0.3728, respectively. The true contrast in the difference image is 1.3, while the contrast achieved in the difference image is 0.2073.

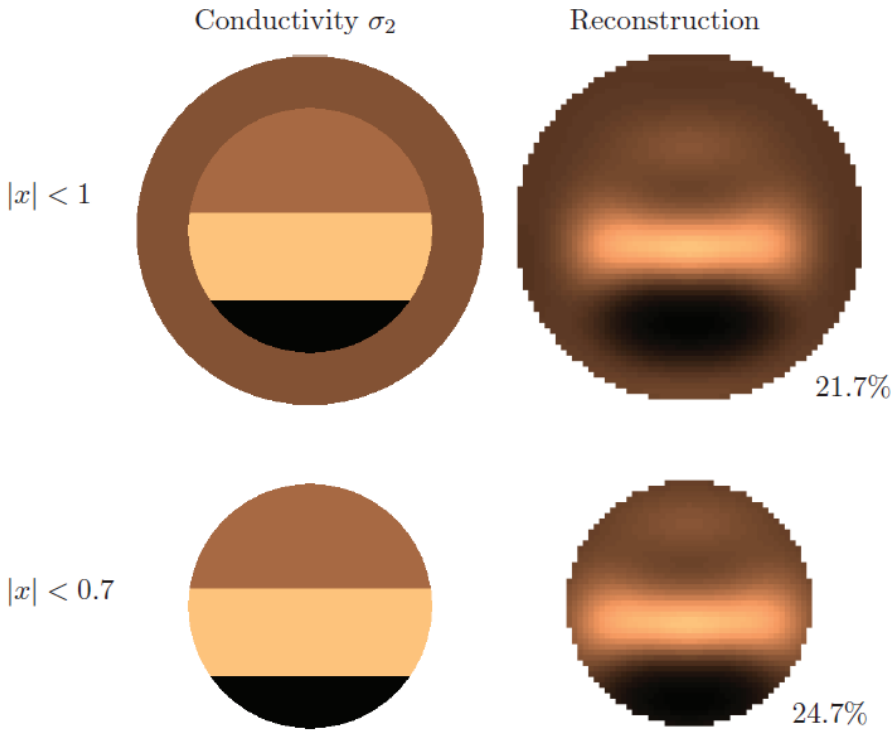

Figure 4. Reconstruction of σ_4 using cutoff frequency $R = 6$ and four values of z_0: real ± 1.4 and purely imaginary $\pm 1.4i$. The four reconstructions have been combined using formula (6.2). In the upper plots the full domain and full reconstruction are displayed; the relative error percentage is computed using formula (6.1). In the lower plots, the outer annulus is removed so that the reconstruction can be analyzed in the region of interest. The relative error percentage 24.7% is computed using formula (6.1) with Ω replaced by the disc $|x| < 0.7$. In the region of interest, the minimum conductivity in the reconstruction is 0.3048, while the true value is 0.3, and the maximum conductivity in the reconstruction is 2.5743, while the true value is 2. The colormaps in all four images are the same, so colors (conductivity values) are directly comparable.